catalysts

MDPI

Article

A Zn-Doped $Ba_{0.5}Sr_{0.5}Co_{0.8}Fe_{0.2}O_{3-\delta}$ Perovskite Cathode with Enhanced ORR Catalytic Activity for SOFCs

Qiannan Zeng [1], Xiaozhen Zhang [1,2,*], Wei Wang [1], Dandan Zhang [1], Yuhua Jiang [1], Xiaojian Zhou [1] and Bin Lin [3]

[1] School of Materials Science and Engineering & Key Laboratory of Inorganic Membranes, Jingdezhen Ceramic Institute, Jingdezhen 333403, China; zengqiannan1225@163.com (Q.Z.); weiwang9411@163.com (W.W.); zhangdandan555555@163.com (D.Z.); jiangyuhua@jci.edu.cn (Y.J.); zhouxiaojian157@163.com (X.Z.)

[2] Jiangxi Provincial Key Laboratory of Fuel Cell Materials and Devices, Jingdezhen 333001, China

[3] School of Materials and Energy, University of Electronic Science and Technology of China, Chengdu 611731, China; bin@mail.ustc.edu.cn

* Correspondence: zhangxiaozhen@jci.edu.cn; Tel. & Fax: +86-798-8499328

Received: 26 January 2020; Accepted: 13 February 2020; Published: 15 February 2020

Abstract: The insufficient oxygen reduction reaction activity of cathode materials is one of the main obstacles to decreasing the operating temperature of solid oxide fuel cells (SOFCs). Here, we report a Zn-doped perovskite oxide $Ba_{0.5}Sr_{0.5}(Co_{0.8}Fe_{0.2})_{0.96}Zn_{0.04}O_{3-\delta}$ (BSCFZ) as the SOFC cathode, which exhibits much higher electrocatalytical activity than $Ba_{0.5}Sr_{0.5}Co_{0.8}Fe_{0.2}O_{3-\delta}$ (BSCF) for the oxygen reduction reaction (ORR). The BSCFZ cathode exhibited a polarization resistance of only 0.23 and 0.03 $\Omega \cdot cm^2$ on a symmetrical cell at 600 and 750 °C, respectively. The corresponding maximum power density of 0.58 $W \cdot cm^{-2}$ was obtained in the yittria-stabilized zirconia (YSZ)-based anode-supported single cell at 750 °C, an increase by 35% in comparison to the BSCF cathode. The enhanced performance can be attributed to a better balance of oxygen vacancies, surface electron transfer and ionic mobility as promoted by the low valence Zn^{2+} doping. This work proves that Zn-doping is a highly effective strategy to further enhance the ORR electrocatalytic activity of state-of-the-art $Ba_{0.5}Sr_{0.5}Co_{0.8}Fe_{0.2}O_{3-\delta}$ cathode material for intermediate temperature SOFCs.

Keywords: solid oxide fuel cells; oxygen vacancy; oxygen reduction reaction; cathode; polarization resistance

1. Introduction

Solid oxide fuel cells (SOFCs) have been gaining increasing attention in the past several decades because of their advantages of environmentally friendly power generation with good fuel flexibility and high energy conversion efficiency [1–6]. Nowadays, reducing the operating temperature of SOFCS to the intermediate-to-low temperature range (400–750 °C) is one of the most significant problems to be solved in order to promote their commercial applications [6–8]. Such a reduction can bring about many advantages, such as decreased material degradation, improved structural stability, ease of sealing, longer service life and much lower operational and system costs [9,10]. However, the lower operating temperature would cause a rapid increment of cathode polarization resistance and resultant sluggish cathode catalytic kinetics for oxygen reduction reaction (ORR), as is a major obstacle to intermediate-to-low temperature SOFC performance improvement [8–10]. Therefore, it is vital to develop cathode materials with excellent ORR electrocatalytic activity and stability for application at reduced temperatures. Many mixed ionic-electronic conductors (MIECs), including the perovskite structures $La_{0.6}Sr_{0.4}Co_{0.8}Fe_{0.2}O_{3-\delta}$ (LSCF) [11], $Ba_{0.5}Sr_{0.5}Co_{0.8}Fe_{0.2}O_{3-\delta}$ (BSCF) [1,10],

$Sm_{0.5}Sr_{0.5}CoO_{3-\delta}$ (SSC) [12] and layered perovskite structure $LnBaCo_2O_{5+\delta}$ [13] have been explored as cathode materials for intermediate-to-low temperature SOFCs. The newly developed perovskite $BaCo_{0.4}Fe_{0.4}Zr_{0.1}Y_{0.1}O_{3-\delta}$ and $SrCo_{0.8}Nb_{0.1}Ta_{0.1}O_{3-\delta}$ cathodes also been proved to have excellent ORR activity at intermediate-to-low temperatures [9,14]. Reduced cathode polarization resistance can be achieved for these MIECs due to their increased number of active sites for ORR with appreciable amounts of oxygen vacancies and faster oxygen ion transport within the material.

Among these MIECs cathode materials, the perovskite structure cobalt-containing BSCF oxide has attracted tremendous attention because of its excellent ORR activity, and yielded a satisfactory performance as the cathode of SOFCs based on doped CeO_2 electrolyte at reduced temperatures (≤600 °C) [1,6,15–18]. The application of BSCF can effectively extend the triple-phase boundary (TPB) of the cathode due to its high oxygen vacancy concentration, low electrochemical surface exchange resistance and high oxygen ion diffusion rate through the material [19]. Actually, BSCF is also one of the most researched perovskite oxides for preparation of oxygen separation membranes due to its fast O^{2-} transport properties [20–22]. Nevertheless, to assure the practical applications of BSCF cathode, the chemical and structural instabilities at intermediate temperatures is a crucial issue that needs to be addressed [4,23]. Several groups has attempted to obtain the stable cubic crystal structure of BSCF by partially substituting the reducible B-site Fe and Co ions with less reducible or constant valence metal ions (e.g., Mo^{6+}, Nb^{3+}, Zr^{4+}, Y^{3+}) [24–30]. The B-site Zn-doping was also found to stabilize the cubic perovskite oxides, e.g., $Ba_{0.5}Sr_{0.5}Zn_{0.2}Fe_{0.8}O_{3-\delta}$ and $BaCo_{0.4}Fe_{0.4}Zn_{0.2}O_{3-\delta}$, thus conferring stable long-term oxygen permeability and CO_2-resistance for the derived ceramic membranes [28,31]. Moreover, Zn-doped BSCF as $Ba_{0.5}Sr_{0.5}(Co_{0.8}Fe_{0.2})_{1-x}Zn_xO_{3-\delta}$ (x = 0~0.15) has been explored in our previous work, and the obtained membrane exhibited a higher oxygen flux, which was mostly attributed to higher concentration of oxygen vacancies as a function of Zn content [20]. In particular, 4mol% Zn (x = 0.04) doping in B-site results in an increment of the oxygen flux by 49%~97% at 700~750 °C.

Herein, we adopted a minor zinc doping strategy to further improve the ORR catalytic activity and stability of $Ba_{0.5}Sr_{0.5}Co_{0.8}Fe_{0.2}O_{3-\delta}$ (BSCF) perovskite as a cathode for SOFCs. The area-specific resistance (ASR) and ORR catalytic activity of 4mol% Zn doped $Ba_{0.5}Sr_{0.5}Co_{0.8}Fe_{0.2}O_{3-\delta}$ (BSCFZ) cathode in the intermediate temperature range was evaluated on $Gd_{0.2}Ce_{0.8}O_{2-\delta}$ (GDC) electrolyte. The electrochemical properties and stability of anode-supported single cells with BSCFZ as cathode have been explored. The single cell was fabricated with the state-of-the-art YSZ electrolyte and Ni-YSZ anode. A GDC buffer layer was applied between the cathode and electrolyte membrane in order to avoid possible chemical interactions between BSCFZ and YSZ.

2. Results and Discussion

Figure 1a,b show the X-ray diffraction (XRD) Rietveld refinement patterns of BSCF and BSCFZ powders, respectively. The refinement results show that both powders possess a cubic perovskite phase structure which can be indexed to the space group $Pm\bar{3}m$ [32]. The deduced lattice parameter (a) of BSCF was 3.982(0) Å, which is comparable to those reported [32,33], and it increased to 3.995(4) Å after Zn-doping. This was mainly ascribed to the larger ionic radius of doped Zn (0.74 Å) than Co (0.53–0.65 Å) and Fe (0.55–0.78 Å), for which the ionic radius varies according to the valence state and spin state. Furthermore, after partial replacing of Co and Fe by Zn, the average valence of B site in BSCF decreased since Co and Fe commonly possess higher valence states of 3+ or 4+ [34,35]. This would result in higher oxygen vacancy concentration of perovskite oxides and consequently caused the lattice expansion to some extent, which is favorable for promoting the surface oxygen exchange and O^{2-} transportation [20]. Figure 1c,d present high-resolution electron transmission microscopy (HR-TEM) images of BSCF and BSCFZ samples with crystalline characteristics. It was found that the (110) plane lattice spacing increases from 0.2816 to 0.2825 nm, further proves that the lattice expansion occurred after Zn^{2+} partially doping into the B-site of BSCF, as is in accordance with the XRD refinement results.

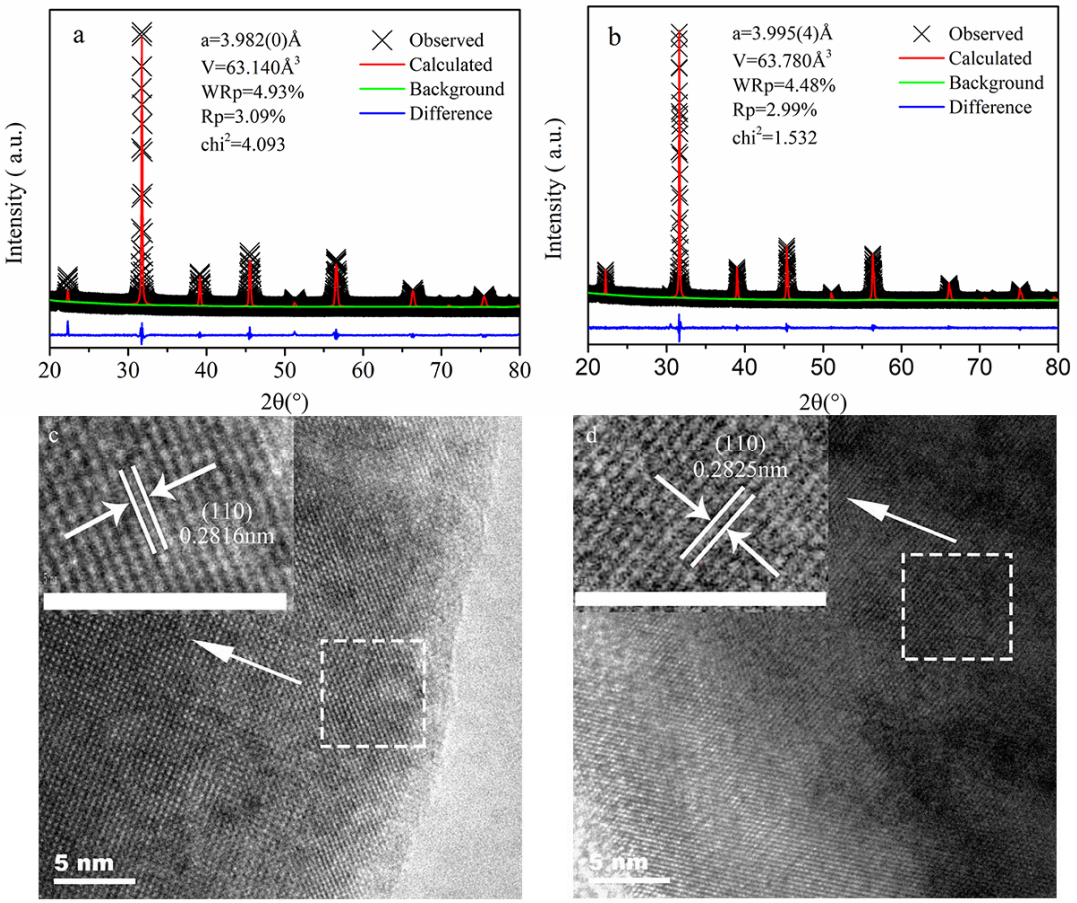

Figure 1. (**a**,**b**) XRD results and (**c**,**d**) HR-TEM images of cathode powders: (**a**,**c**) BSCF and (**b**,**d**) BSCFZ. Rp, WRp and chi^2 in Figure 1a,b indicates the overall degree of fitting, weighted Rp and the goodness of fitting, respectively.

XRD analysis of BSCF-GDC and BSCFZ-GDC mixtures (50:50 in mass ratio) calcined at 1050 °C for 6 h under air atmosphere was also conducted to evaluate the chemical compatibility of cathode materials and GDC buffer layer. As can be observed in Figure 2, the XRD results indicate respective phases of the GDC, BSCFZ, and BSCF without the formation of impurities, suggesting good chemical compatibility with each other even at a temperature much higher than the operating temperature (≤750 °C).

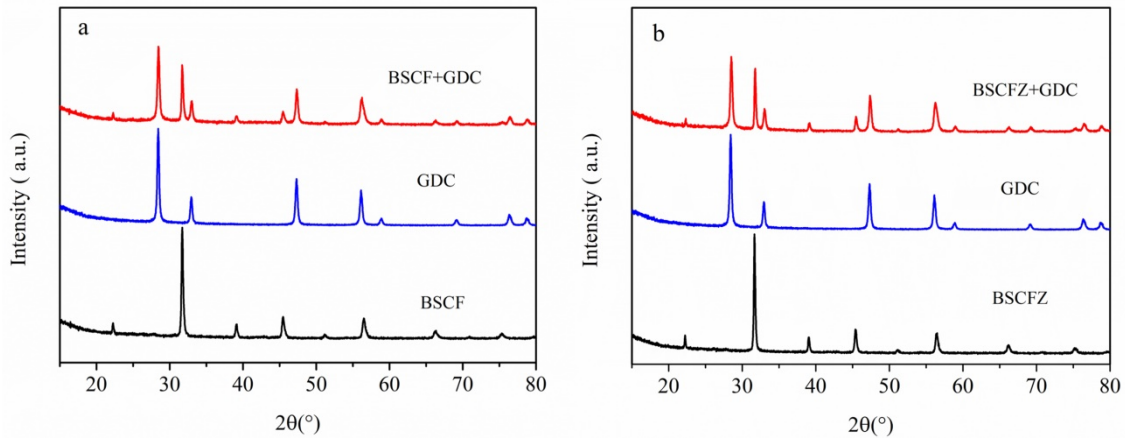

Figure 2. XRD patterns of (**a**) BSCF-GDC and (**b**) BSCFZ-GDC mixtures heat-treated at 1050 °C for 6 h in air.

Figure 3a,b demonstrates the influences of temperature on the electrical conductivity of BSCF and BSCFZ materials measured in air. The total electrical conductivity of BSCF agrees with those reported in the literature [36,37]. Two different conductivity regions with different activation energies can be observed for both compositions. In the low-temperature region, the conductivity shows an increase with temperature up to about 500 °C, whereas the conductivity decreases slightly or keeps almost constant at temperatures higher than 500 °C. Generally, the conductive behavior of BSCF and BSCFZ as MIECs is mostly dominated by the p-type small polaron hopping mechanism, since their electronic conductivity is one to two orders of magnitude higher than the ionic conductivity. The temperature dependence of conductivity correlated reasonably well with the generation of oxygen vacancies in different temperature range for BSCF and BSCFZ (Figure 3c). In the low-temperature range (<400 °C in this case) with almost unchanged oxygen vacancy concentration, the concentration of p-type charge carrier (electron hole) is nearly constant, while the hole mobility is thermally activated which resulted in enhanced electronic conductivity with temperature. At temperatures above 400 °C, on the one hand, the increase of oxygen vacancy ($V_o^{\cdot\cdot}$) concentration with temperature resulted in a decrease of the electron hole ($h\cdot$) concentration and thus the electronic conductivity. This process can be described by the reversible defect reaction using Kröger-Vink notation, as shown in Equation (1) [37]. On the other hand, the positive effect of increased small polaron mobility with temperature and improved oxygen ionic conductivity counteract the decrease in electronic conductivity. The temperature-dependent balance of electron hole and oxygen vacancy concentration led to a maximum value of total conductivity at ~500 °C.

$$V_o^{\cdot\cdot} + \frac{1}{2}O_2(g) \leftrightarrow O_O^x + 2h^{\cdot} \quad (1)$$

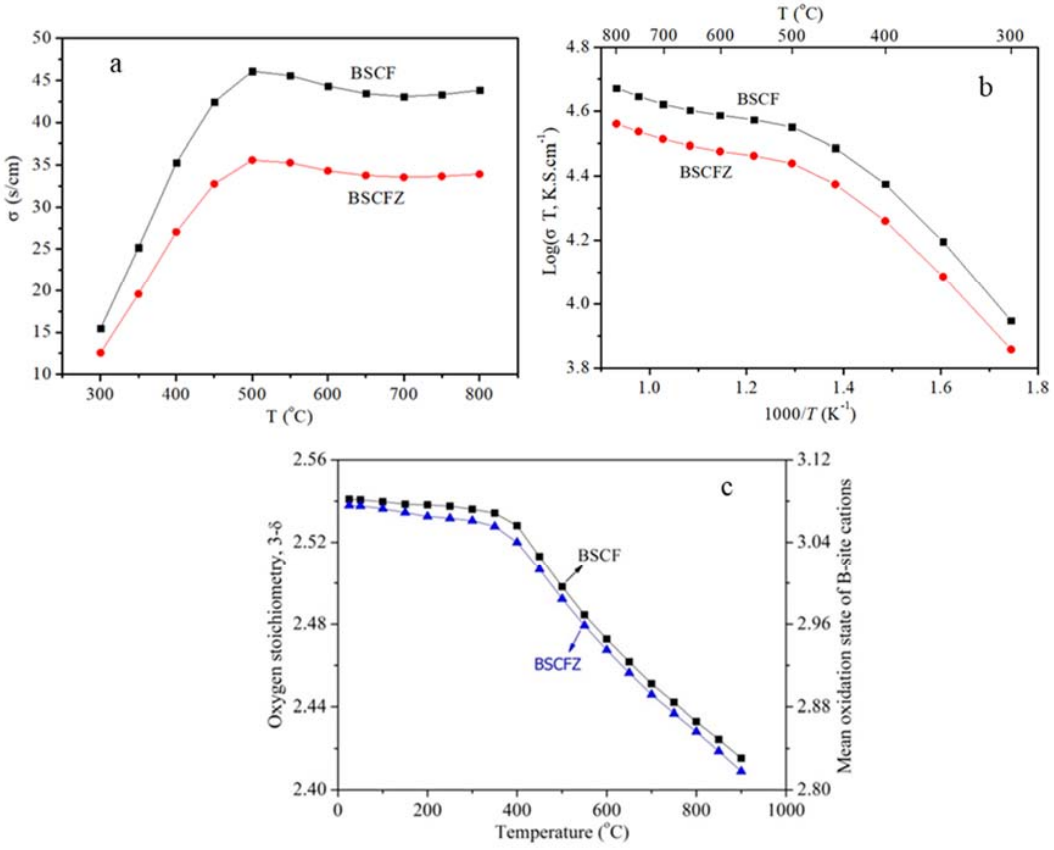

Figure 3. Influences of temperature on electrical conductivity (**a**): linear plot; (**b**): Arrhenius plot and (**c**): oxygen stoichiometry of BSCF and BSCFZ materials in air.

As shown in Figure 3a,b, the Zn doping in B-site led to decreased total conductivity with maximum value being 46.4 and 35.6 S/cm for BSCF and BSCFZ, respectively. This can be ascribed to enhanced

oxygen vacancy concentration and thus decreased B-site cations average valence as shown in Figure 3c, since partial Fe and Co commonly have higher valence states of 3+ or 4+. To further explore the influence of Zn-doping on B-site cations oxidation state, X-ray photoelectron spectrometer (XPS) analysis was also performed for BSCF and BSCFZ. Figure 4a,b show the core-level XPS spectra of Co 2p and Fe 2p. As shown in Figure 4a, four components can be obtained by deconvoluting the Co2p spectra of both samples, which were attributed to Co $2p_{1/2}$ and Co $2p_{3/2}$, respectively. The peaks at 778.96 and 794.19 eV can be assigned to Co^{3+}, while the peaks at 780.88 and 796.01 eV could be assigned to Co^{4+}, assuming that Co^{3+} and Co^{4+} were the main valence states of Co [34,35]. The Co $2p_{3/2}$–Co $2p_{1/2}$ energy splitting (~15.2 eV) was consistent with those reported. However, it must be noted that this does not exclude the existence of Co^{2+}, since the peaks for Co^{2+} are generally considered to overlap with the peaks for Co^{3+}, Co^{4+} and Ba^{2+} [38]. Therefore, it is very challenging to quantitatively determine the surface Co valence by fitting the Co 2p peaks. Despite this, it can be inferred that Co^{3+} would be the main valence states, since the average valence of B-site deduced from oxygen stoichiometry (3-δ) was close to 3 at room temperature as shown in Figure 3c. It can be found from Figure 4b, the peak intensities of Fe 2p in both samples are weak due to low Fe content. Deconvolution of the Fe 2p peaks indicates that both Fe^{3+} and Fe^{2+} exist, and the satellite peak at ~717.5 suggests that Fe^{3+} is the main form [34].

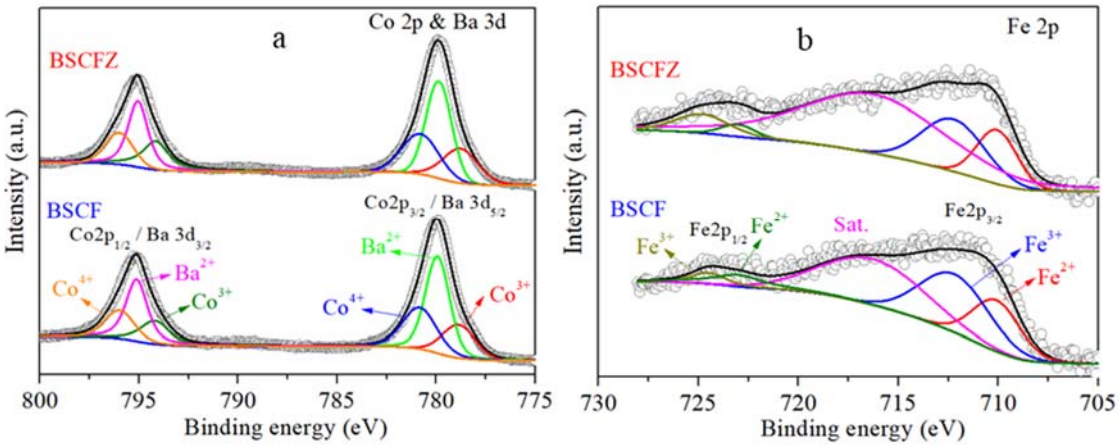

Figure 4. XPS spectra of (**a**) Co 2p and Ba 3d, and (**b**) Fe 2p core levels of BSCF and BSCFZ powders.

Figure 5 shows the area-specific polarization resistance (R_p) and corresponding Arrhenius plot of BSCF and BSCFZ cathodes on GDC electrolyte-supported symmetrical cells tested at 600~750 °C in air. As can be seen, the R_p of both cathodes increases obviously with the decrease of operational temperature. However, BSCFZ cathode exhibited much lower R_p compared with BSCF cathode, and the difference incremented from 0.01 Ω·cm^2 at 750 °C to 0.22 Ω·cm^2 at 600 °C, indicating a R_p reduction of 25%~49% for BSCFZ cathode. The obtained R_p of BSCFZ cathode is also much smaller than that of BSCF cathode for 0.121~1.424 Ω·cm^2 and $La_{0.8}Sr_{0.2}MnO_{3-\delta}$ (LSM) coated BSCF cathode for 0.09~1.414 Ω·cm^2 at 600~750 °C reported by Qiu et al. [23] and BSCF-GDC composite cathode for 0.79 Ω·cm^2 at 700 °C [39], and comparable to that of $Ba_{0.5}Sr_{0.5}Co_{0.8}Fe_{0.1}Nb_{0.1}O_{3-\delta}$ cathode (0.02 Ω·cm^2 at 750 °C) reported by Li et al. [40]. The Arrhenius plot of BSCFZ and BSCF cathode Rp are presented in Figure 5b. The derived ORR activation energy (Ea) of BSCFZ cathode is about 99.68 kJ·mol^{-1}. This value is much lower than that of BSCF cathode (about 120.05 kJ·mol^{-1}), which is close to that of BSCF and LSM coated BSCF cathodes (116~123.5 kJ·mol^{-1}) obtained by Shao et al. and Qiu et al. [1,23]. The enhanced ORR activity and thus reduced polarization resistance of BSCFZ cathode are mostly attributed to higher oxygen vacancy concentration and oxygen permeability originated from Zn-doping, which promoted the oxygen surface exchange, oxygen reduction and O^{2-} ions transportation [15,19,20].

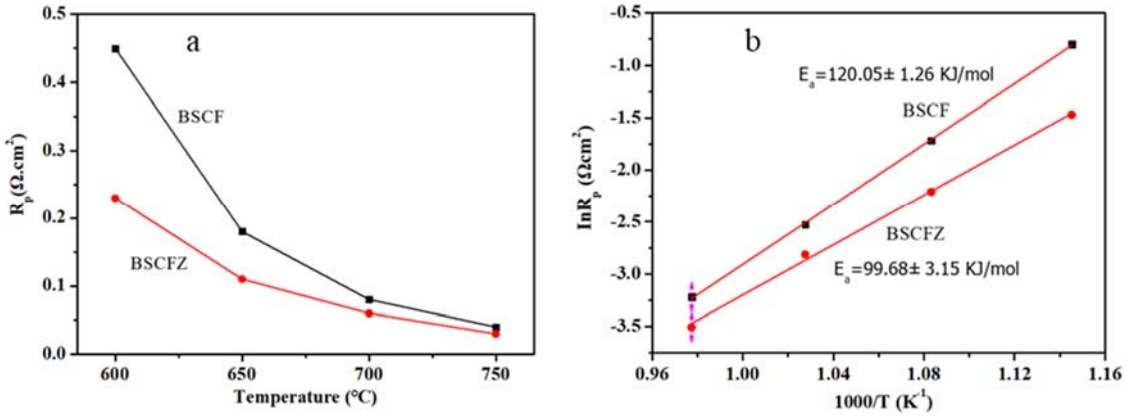

Figure 5. (**a**) Polarization resistances (Rp) and (**b**) corresponding Arrhenius plot of BSCF and BSCFZ cathodes of symmetrical cells measured at 600~750 °C.

Figure 6 presents the current-voltage (*I-V*) and current-power (*I-P*) characteristic curves of the single cells with BSCF and BSCFZ cathodes. As can be seen, all the open circuit voltage (OCV) values (1.05~1.08 V) of cells are close to the theoretical value by Nernst equation, indicating the electrolyte layer is dense enough. The cell with BSCFZ cathode achieved the maximum power densities of approximately 0.58, 0.41, 0.25 W·cm^{-2} at 750, 700 and 650 °C (Figure 6b), respectively, which contributes to an increase by 35%~41% as compared to that of cell with BSCF cathode, being 0.43, 0.29 and 0.18 W·cm^{-2} (Figure 6a), respectively. The significant enhancement of single cell power output after minor Zn-doping in the cathode mainly resulted from better cathode ORR activity and thus lower polarization resistance as shown in Figures 5 and 7, since the anode and electrolyte thin films were fabricated using the same procedure. It is worth noting that the achieved power density of the single cell with BSCFZ cathode at 750 °C is three times higher than that of the single cell with BSCF-GDC composite cathode possessing similar cell structure and close YSZ electrolyte thickness (~8 μm) [39], and even higher than that of the cell with BSCF cathode (only 0.45 W·cm^{-2} at 800 °C) derived from a screen-printing method [3].

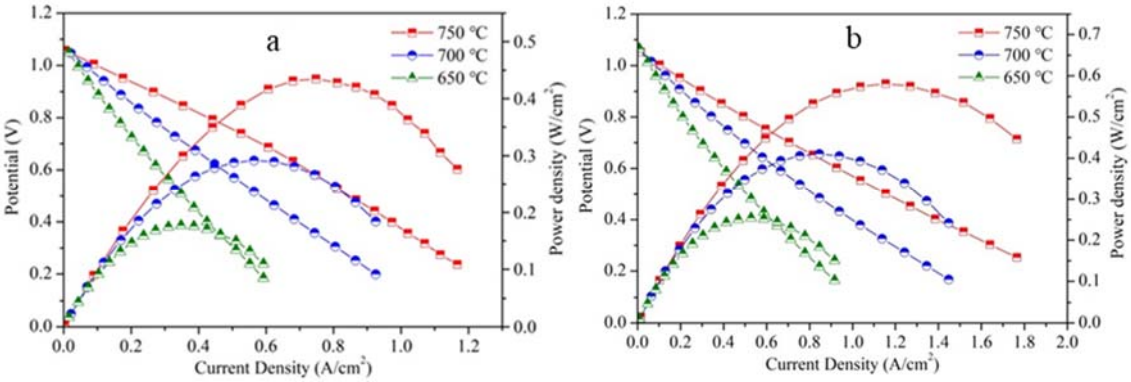

Figure 6. *I-V* and *I-P* curves of the fuel cells with (**a**) BSCF and (**b**) BSCFZ cathodes measured at 650–750 °C.

To further investigate the effect of minor Zn-doping on the BSCF cathode performance, the electrochemical impedance spectra (EIS) of the anode-supported single cells were tested at 750, 700 and 650 °C. Figure 7a,b illustrate the obtained impedance results, which is fitted with the equivalent circuit based on the electrochemical process as shown in Figure 7c using the Z-view program, in which L and R_o correspond to the cable inductance and the total ohmic resistance, respectively; R_1 is the charge-transfer resistance, which is associated with the oxygen-ion (O^{2-}) and charge transfer at the electrode and electrode/electrolyte interface (high frequency arc); R_2 mainly corresponds to the

resistance (low frequency arc) of the oxygen surface exchange and diffusion process, which is related to the concentration of oxygen vacancy and the microstructure of the electrode [41,42].

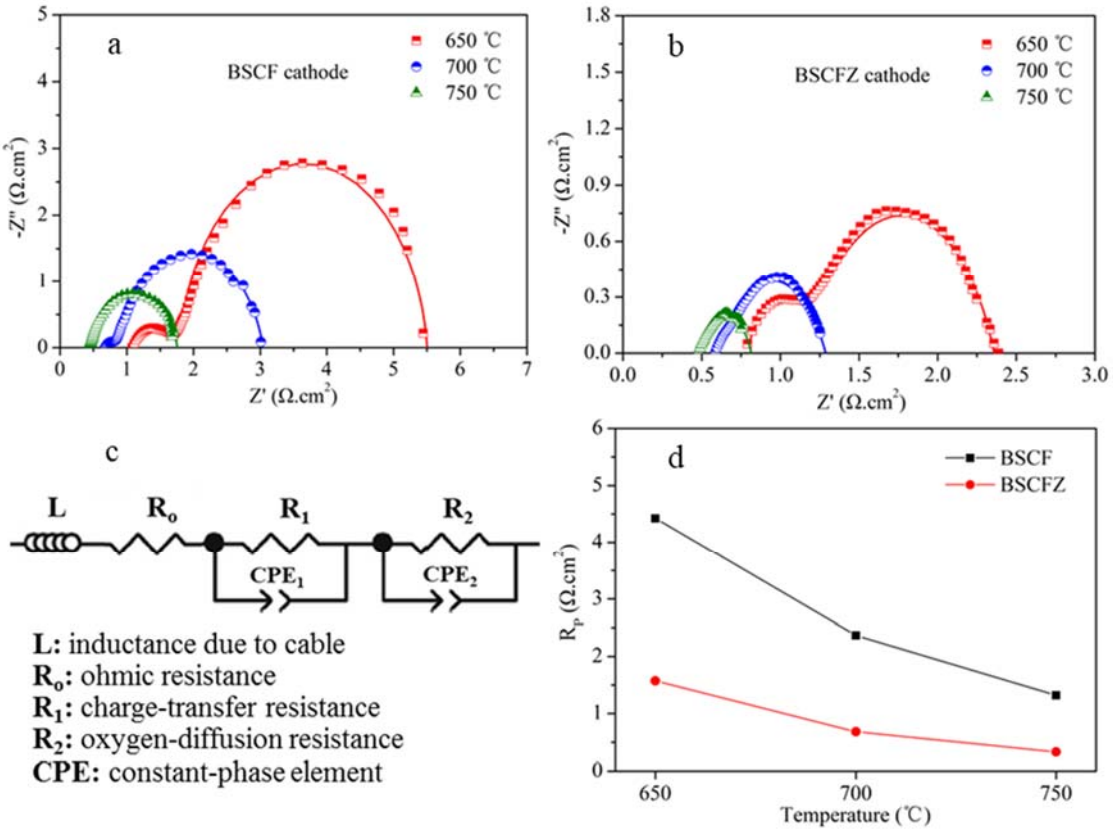

Figure 7. Impedance spectra of single cells with (**a**) BSCF and (**b**) BSCFZ cathodes at 650, 700 and 750 °C, (**c**) equivalent circuit applied to fit the impedance data and (**d**) summarized R_p from (**a**,**b**) as a function of temperature.

In consideration that the anode polarization was generally minor, the polarization resistance (R_p) of single cell could be thus mostly ascribed to the cathode polarization. Figure 7d shows the R_p values of single cells with both BSCF and BSCFZ cathodes as a function of the operating temperature. The R_p value for both cells decreases with increasing temperature, and the doping of minor Zn into BSCF cathode leads to a significant reduction of R_p, manifesting that the O^{2-} transfer and the oxygen-reduction and diffusion processes were promoted due to incremented oxygen vacancy concentration and ORR activity of BSCFZ cathode. Furthermore, as can be observed in Figure 7b, R_1 reduces with the increase of temperature, and becomes negligible at 700 and 750 °C, indicating that the Zn-doping benefits the O^{2-} transfer in BSCF-based cathode. However, R_2 is predominant in the impedance spectra, suggesting the single cell property could be further enhanced by optimizing the microstructure of electrodes to facilitate the mass transportation. In general, the AC impedance results of the single cells were in good agreement with their power densities.

The stability of single cell with BSCFZ cathode was tested at 750 °C for 140 h under a constant voltage of 0.7 V. Figure 8 presents the obtained current density of single cell as a function of run time. For comparison, the result for single cell with BSCF cathode was also included. The cell current density with BSCFZ cathode remained nearly unchanged except for slight increase in the initial dozens of hours due to the cathode activation process at elevated temperature. In contrast, for the cell with BSCF cathode, the current density at 750 °C decreased by about 24% after run for 140 h. This improved cell stability can be ascribed to better phase stability of cubic perovskite structure BSCFZ and good cathode/electrolyte interface bonding as shown in Figure 9b.

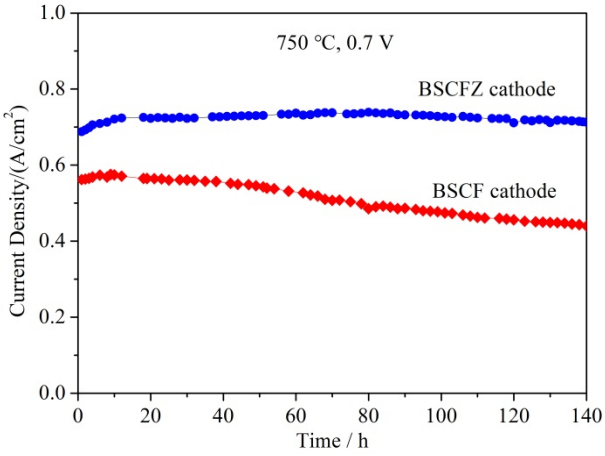

Figure 8. Current density variation trend of the single cells with BSCFZ and BSCF cathodes at 750 °C running for 140 h under 0.7 V.

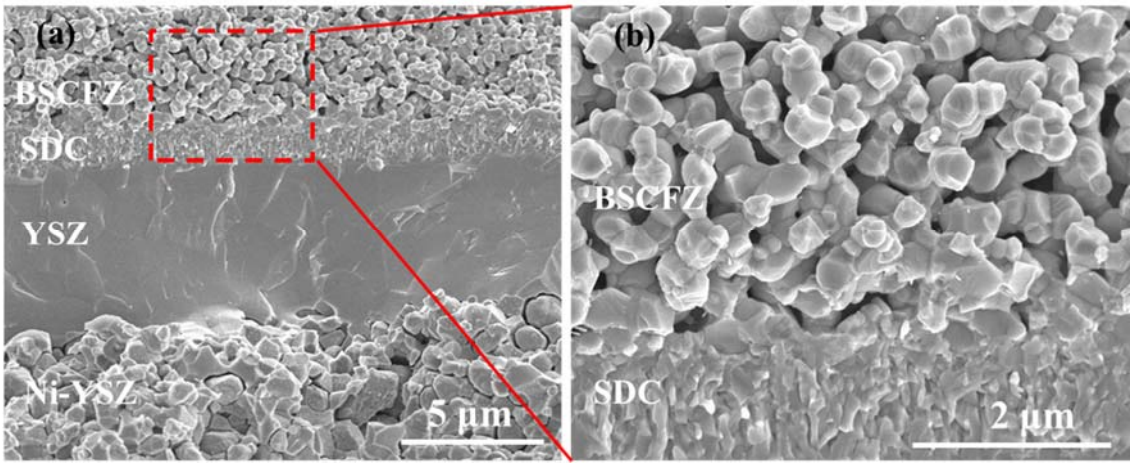

Figure 9. Cross-sectional SEM images of anode-supported Ni-YSZ/YSZ/GDC/ BSCFZ single cell after tests: (**a**) over view and (**b**) BSCFZ/ GDC interface.

Figure 9 shows the cross-sectional field emission scanning electron microscopy (FE-SEM) images of the single cell with BSCFZ cathode after short-term test. As can be observed in Figure 9a, the YSZ electrolyte layer (about 8 μm in thickness) is dense enough, and exhibits excellent interfacial bonding with both the Ni-YSZ anode and the GDC barrier layer. It can also be found from Figure 9b that the GDC buffer layer (about 2 μm in thickness) and porous BSCFZ cathode are well bonded to each other after test, and no sign of delamination was observed. The GDC functional layer is used to improve the interface of cathode and electrolyte. The porous structure of cathode would facilitate the transportation of oxygen and increment the active sites for ORR to improve the cell performance.

3. Materials and Methods

3.1. Powder synthesis

$Ba_{0.5}Sr_{0.5}(Co_{0.8}Fe_{0.2})_{1-x}Zn_xO_{3-\delta}$ powders ($x = 0$ and 0.04, denoted as BSCF and BSCFZ, respectively) were synthesized by the modified Pechini method as reported elsewhere [6]. All the reagents were purchased from Sinopharm Chemical Reagent Co., Ltd (Shanghai, China) and used without further purification. Metal nitrates at stoichiometric ratio were dissolved, and citric acid as complexing agent was then added under constant stirring. Diluted $NH_3 \cdot H_2O$ was added to adjust the pH value at ~7. The molar ratio of citric acid to metal ion was set at 1.5. The mixed metal ions solution was heated under constant stirring to evaporate water until it became viscous gel and finally self-ignited to turn

into the black ash. The ash was calcined at 950 °C for 3 h to obtain ultrafine BSCF and BSCFZ powders. The GDC and YSZ powders were obtained with the same method, which were calcined at 800 °C for 2 h.

3.2. Cell preparation

The dense GDC electrolyte discs were fabricated by dry-pressing technique, followed by sintering at 1450 °C for 10 h. The symmetric cells with the configuration of cathode (~15 μm)/GDC (~0.5 mm) /cathode (~15 μm) were fabricated to measure the cathodic area-specific resistance. Fine BSCFZ or BSCF powder was fully mixed with ethyl cellulose-terpineol binder to prepare the cathode inks. The BSCFZ (or BSCF) ink was screen-printed on both sides of polished GDC discs and calcined at 1000 °C for 3 h to form a porous cathode. To assemble a half-cell with NiO-YSZ/YSZ/GDC three-layer structure, the NiO-YSZ/YSZ double-layer unit was co-pressed with starch as pore-forming agent, followed by slurry coating of GDC, and co-sintered at 1450 °C for 10 h. Finally, the cathode ink was screen-printed on GDC layer surface of the half-cell and calcined at 1000 °C for 3 h to obtain the anode-supported single cells.

3.3. Characterization

The phase structure of the powders was identified by XRD (D8 Advance, Bruker, Ettlingen, Germany) with Cu K_α radiation. XRD Rietveld refinement was performed using GSAS software. HR-TEM (JEM-2010, JEOL, Tokyo, Japan) in conjunction with selected area electron diffraction was also used for phase identification of cathode powders. The conductivity was tested applying a DC four-terminal method in air with a digital multimeter (Keithley 2001, Keithley, Cleveland, OH, USA). Before measurement, dense bar-shaped samples were prepared by dry-pressing and subsequent sintering at 1150 °C for 5 h. The oxygen vacancy concentration from 25 to 900 °C was measured by the combination of thermogravimetric analysis (TGA, TGA/DSC 1, Mettler Toledo, Zurich, Switzerland) and iodometric titration as described in the reference [20]. XPS (MULT1LAB2000, VG, Waltham, MA, USA) with Al K_α radiation source was applied to analyze the element state of cathode materials, and spectrum calibration was performed by taking the C1s electron peak (BE = 284.8 eV) as the reference peak. The microstructure of single cells was obtained through FE-SEM (SU-8010, Hitachi, Tokyo, Japan). Electrochemical analysis of symmetric cells and single cells was performed using an electrochemical workstation (Zennium Pro, Zahner-elektrik, Kronach, Germany) to obtain the impedance spectra and current-voltage curves. The cell measurements were conducted at 600–750 °C with H_2/3% H_2O as the fuel (100 mL/min) and ambient air as the oxidant.

4. Conclusions

The B-site 4 mol% Zn-doped BSCF oxide with stable cubic perovskite structure was prepared and investigated as the cathode material of intermediate temperature SOFCs. Zn-doping led to increased lattice parameters and oxygen vacancy concentration for BSCF material. The prepared BSCFZ cathode exhibited significantly enhanced ORR electrocatalytic activity with the area-specific polarization resistance reduction of 25~49% compared to BSCF cathode at 600~750 °C. It has been demonstrated that the BSCFZ cathode material has excellent electrochemical performance as well as short-term stability. For the single cell with BSCFZ cathode, maximum power densities of 0.58, 0.41, 0.25 $W{\cdot}cm^{-2}$ were obtained at 750, 700 and 650 °C, respectively, showing an increase of 35~41% as compared to that obtained with the BSCF cathode. The cell with BSCFZ cathode demonstrated no obvious performance decay under a voltage load of 0.7 V at 750 °C after running for 140 h. Our findings manifest that BSCFZ is a potential cathode material for YSZ-based SOFCs working in the intermediate temperature range.

Author Contributions: Data curation, Q.Z. and Y.J.; Formal analysis, Q.Z., W.W.; Funding acquisition, X.Z. (Xiaozhen Zhang); Investigation, Q.Z. and W.W.; Methodology, X.Z. (Xiaojian Zhou); Project administration, X.Z. (Xiaozhen Zhang) and Y.J.; Resources, W.W. and Y.J.; Software, D.Z. and X.Z. (Xiaojian Zhou); Supervision, X.Z.

(Xiaozhen Zhang) and B.L.; Writing—original draft, Q.Z. and D.Z.; Writing—review & editing, X.Z. (Xiaozhen Zhang) and B.L. All authors have read and agreed to the published version of the manuscript.

Funding: This work was financially supported by the National Natural Science Foundation of China under contract No. 51462012 and Jiangxi Provincial Department of Education, China (GJJ170783, KJLD14076).

Conflicts of Interest: The authors declare no conflict of interest.

References

1. Shao, Z.; Haile, S.M. A high-performance cathode for the next generation of solid-oxide fuel cells. *Nature* **2004**, *431*, 170–173. [CrossRef]
2. Zhang, X.; Jiang, Y.; Hu, X.; Sun, L.; Ling, Y. High Performance Proton Conducting Solid Oxide Fuel Cells with a Layered Perovskite $GdBaCuCoO_{5+x}$ Cathode. *Electron. Mater. Lett.* **2018**, *14*, 147–153. [CrossRef]
3. Liu, B.; Chen, X.; Dong, Y.; Mao, S.S.; Cheng, M. A High-Performance, Nanostructured $Ba_{0.5}Sr_{0.5}Co_{0.8}Fe_{0.2}O_{3-\delta}$ Cathode for Solid-Oxide Fuel Cells. *Adv. Energy Mater.* **2011**, *1*, 343–346. [CrossRef]
4. Kim, J.; Choi, S.; Jun, A.; Jeong, H.Y.; Shin, J.; Kim, G. Chemically stable perovskites as cathode materials for solid oxide fuel cells: La-doped $Ba_{0.5}Sr_{0.5}Co_{0.8}Fe_{0.2}O_{3-\delta}$. *ChemSusChem* **2014**, *7*, 1669–1675. [CrossRef] [PubMed]
5. Liu, Q.; Dong, X.; Xiao, G.; Zhao, F.; Chen, F. A Novel Electrode Material for Symmetrical SOFCs. *Adv. Mater.* **2010**, *22*, 5478–5482. [CrossRef] [PubMed]
6. Lin, B.; Ding, H.; Dong, Y.; Wang, S.; Zhang, X.; Fang, D.; Meng, G. Intermediate-to-low temperature protonic ceramic membrane fuel cells with $Ba_{0.5}Sr_{0.5}Co_{0.8}Fe_{0.2}O_{3-\delta}$ –$BaZr_{0.1}Ce_{0.7}Y_{0.2}O_{3-\delta}$ composite cathode. *J. Power Sources* **2009**, *186*, 58–61. [CrossRef]
7. Kan, W.H.; Samson, A.J.; Thangadurai, V. Trends in electrode development for next generation solid oxide fuel cells. *J. Mater. Chem. A* **2016**, *4*, 17913–17932. [CrossRef]
8. Qiu, P.; Li, J.; Jia, L.; Chi, B.; Pu, J.; Li, J.; Chen, F. $LaCoO_{3-\delta}$ coated $Ba_{0.5}Sr_{0.5}Co_{0.8}Fe_{0.2}O_{3-\delta}$ cathode for intermediate temperature solid oxide fuel cells. *Electrochim. Acta* **2019**, *319*, 981–989. [CrossRef]
9. Li, M.; Zhao, M.; Li, F.; Zhou, W.; Peterson, V.K.; Xu, X.; Shao, Z.; Gentle, I.; Zhu, Z. A niobium and tantalum co-doped perovskite cathode for solid oxide fuel cells operating below 500 °C. *Nat. Commun.* **2017**, *8*, 13990. [CrossRef]
10. Xu, X.; Wang, H.; Fronzi, M.; Wang, X.; Bi, L.; Traversa, E. Tailoring cations in a perovskite cathode for proton-conducting solid oxide fuel cells with high performance. *J. Mater. Chem. A* **2019**, *7*, 20624–20632. [CrossRef]
11. Wang, H.; Zhang, X.; Zhang, W.; Wei, Z.; Guan, K.; Meng, J.; Meng, F.; Meng, J.; Liu, X. Enhancing catalysis activity of $La_{0.6}Sr_{0.4}Co_{0.8}Fe_{0.2}O_{3-\delta}$ cathode for solid oxide fuel cell by a facile and efficient impregnation process. *Int. J. Hydrogen Energy* **2019**, *44*, 13757–13767. [CrossRef]
12. Park, Y.M.; Kim, H. Porous Gd-doped ceria barrier layer on solid oxide fuel cell with $Sm_{0.5}Sr_{0.5}CoO_{3-\delta}$ Cathodes. *Ceram. Int.* **2013**, *39*, 2037–2043. [CrossRef]
13. Tarancón, A.; Burriel, M.; Santiso, J.; Skinner, S.J.; Kilner, J.A. Advances in layered oxide cathodes for intermediate temperature solid oxide fuel cells. *J. Mater. Chem.* **2010**, *20*, 3799–3813. [CrossRef]
14. Wei, K.; Li, N.; Wu, Y.; Song, W.; Wang, X.; Guo, L.; Khan, M.; Wang, S.; Zhou, F.; Ling, Y. Characterization and optimization of highly active and Ba-deficient $BaCo_{0.4}Fe_{0.4}Zr_{0.1}Y_{0.1}O_{3-\delta}$-based cathode materials for protonic ceramics fuel cells. *Ceram. Int.* **2019**, *45*, 18583–18591. [CrossRef]
15. Zhou, W.; Ran, R.; Shao, Z. Progress in understanding and development of $Ba_{0.5}Sr_{0.5}Co_{0.8}Fe_{0.2}O_{3-\delta}$-based cathodes for intermediate-temperature solid-oxide fuel cells: A review. *J. Power Sources* **2009**, *192*, 231–246. [CrossRef]
16. Wei, B.; Lv, Z.; Huang, X.; Miao, J.; Sha, X.; Xin, X.; Su, W. Crystal structure, thermal expansion and electrical conductivity of perovskite oxides $Ba_xSr_{1-x}Co_{0.8}Fe_{0.2}O_{3-\delta}$ ($0.3 \leq x \leq 0.7$). *J. Eur. Ceram. Soc.* **2006**, *26*, 2827–2832. [CrossRef]
17. Chen, Z.; Ran, R.; Zhou, W.; Shao, Z.; Liu, S. Assessment of $Ba_{0.5}Sr_{0.5}Co_{1-y}Fe_yO_{3-\delta}$ (y=0.0-1.0) for prospective application as cathode for IT-SOFCs or oxygen permeating membrane. *Electrochim. Acta* **2007**, *52*, 7343–7351. [CrossRef]

18. Liu, B.; Jia, L.; Ouyang, R.; Li, J. Preparation and Electrochemical Properties of $La_{0.8}Sr_{0.2}MnO_{3-\sigma}$ Coated $Ba_{0.5}Sr_{0.5}C_{o0.8}Fe_{0.2}O_{3-\sigma}$ Cathodes for Intermediate Temperature Solid Oxide Fuel Cells. *J. Ceram.* **2019**, *40*, 99–102. (In Chinese)
19. Liu, B.; Zhang, Y.; Zhang, L. Oxygen reduction mechanism at $Ba_{0.5}Sr_{0.5}Co_{0.8}Fe_{0.2}O_{3-\delta}$ cathode for solid oxide fuel cell. *Int. J. Hydrogen Energy* **2009**, *34*, 1008–1014. [CrossRef]
20. Zhang, X.; Motuzas, J.; Liu, S.; da Costa, J.C.D. Zinc-doped BSCF perovskite membranes for oxygen separation. *Sep. Purif. Technol.* **2017**, *189*, 399–404. [CrossRef]
21. Zhu, J.; Liu, G.; Liu, Z.; Chu, Z.; Jin, W.; Xu, N. Unprecedented perovskite oxyfluoride membranes with high-efficiency oxygen ion transport paths for low-temperature oxygen permeation. *Adv. Mater.* **2016**, *28*, 3511–3515. [CrossRef] [PubMed]
22. Leo, A.; Smart, S.; Liu, S.; da Costa, J.C.D. High performance perovskite hollow fibres for oxygen separation. *J. Membr. Sci.* **2011**, *368*, 64–68. [CrossRef]
23. Qiu, P.; Wang, A.; Li, J.; Li, Z.; Jia, L.; Chi, B.; Pu, J.; Li, J. Promoted CO_2-poisoning resistance of $La_{0.8}Sr_{0.2}MnO_3$-coated $Ba_{0.5}Sr_{0.5}C_{o0.8}Fe_{0.2}O_3$ cathode for intermediate temperature solid oxide fuel cells. *J. Power Sources* **2016**, *327*, 408–413. [CrossRef]
24. Gasparyan, H.; Claridge, J.B.; Rosseinsky, M.J. Oxygen permeation and stability of Mo-substituted BSCF membranes. *J. Mater. Chem. A* **2015**, *3*, 65–18272. [CrossRef]
25. Fang, S.M.; Yoo, C.-Y.; Bouwmeester, H.J.M. Performance and stability of niobium-substituted $Ba_{0.5}Sr_{0.5}Co_{0.8}Fe_{0.2}O_{3-\delta}$ membranes. *Solid State Ionics* **2011**, *195*, 1–6. [CrossRef]
26. Wang, F.; Nakamura, T.; Yashiro, K.; Mizusaki, J.; Amezawa, K. Effect of Nb doping on the chemical stability of BSCF-based solid solutions. *Solid State Ionics* **2014**, *262*, 719–723. [CrossRef]
27. Ravkina, O.; Klande, T.; Feldhoff, A. Investigation of Zr-doped BSCF perovskite membrane for oxygen separation in the intermediate temperature range. *J. Solid State Chem.* **2013**, *201*, 101–106. [CrossRef]
28. Chen, X.; Liu, H.; Wei, Y.; Caro, J.; Wang, H. A novel zincum-doped perovskite-type ceramic membrane for oxygen separation. *J. Alloy. Compd.* **2009**, *484*, 386–389. [CrossRef]
29. Almar, L.; Störmer, H.; Meffert, M.; Szász, J.; Wankmüller, F.; Gerthsen, D.; Ivers-Tiffée, E. Improved Phase Stability and CO_2 Poisoning Robustness of Y-Doped $Ba_{0.5}Sr_{0.5}Co_{0.8}Fe_{0.2}O_{3-\delta}$ SOFC Cathodes at Intermediate Temperatures. *ACS Appl. Energy Mater.* **2018**, *1*, 1316–1327. [CrossRef]
30. Meffert, M.; Unger, L.-S.; Störmer, H.; Sigloch, F.; Wagner, S.F.; Ivers-Tiffée, E.; Gerthsen, D. The effect of B-site Y substitution on cubic phase stabilization in $(Ba_{0.5}Sr_{0.5})(Co_{0.8}Fe_{0.2})O_{3-\delta}$. *J. Am. Ceram. Soc.* **2019**, *102*, 4929–4942. [CrossRef]
31. Wang, H.; Tablet, C.; Feldhoff, A.; Caro, J. A cobalt-free oxygen-permeable membrane based on the perovskite-type oxide $Ba_{0.5}Sr_{0.5}Zn_{0.2}Fe_{0.8}O_{3-\delta}$. *Adv. Mater.* **2005**, *17*, 1785–1788. [CrossRef]
32. Zeng, P.; Chen, Z.; Zhou, W.; Gu, H.; Shao, Z.; Liu, S. Re-evaluation of $Ba_{0.5}Sr_{0.5}Co_{0.8}Fe_{0.2}O_{3-\delta}$ perovskite as oxygen semi-permeable membrane. *J. Membr. Sci.* **2007**, *291*, 148–156. [CrossRef]
33. Shiiba, H.; Bishop, C.L.; Rushton, M.J.D.; Nakayama, M.; Nogami, M.; Kilner, J.A.; Grimes, R.W. Effect of A-site cation disorder on oxygen diffusion in perovskite-type $Ba_{0.5}Sr_{0.5}Co_{1-x}Fe_xO_{2.5}$. *J. Mater. Chem. A* **2013**, *1*, 10345–10352. [CrossRef]
34. Liu, B.; Zhang, Y.; Tang, L. X-ray photoelectron spectroscopic studies of $Ba_{0.5}Sr_{0.5}Co_{0.8}Fe_{0.2}O_{3-\delta}$ cathode for solid oxide fuel cells. *Int. J. Hydrogen Energy* **2009**, *34*, 435–439. [CrossRef]
35. Cui, X.; O'Hayre, R.; Pylypenko, S.; Zhang, L.; Zeng, L.; Zhang, X.; Hua, Z.; Chen, H.; Shi, J. Fabrication of a mesoporous $Ba_{0.5}Sr_{0.5}Co_{0.8}Fe_{0.2}O_{3-\delta}$ perovskite as a low-cost and efficient catalyst for oxygen reduction. *Dalton Trans.* **2017**, *46*, 13903–13911. [CrossRef]
36. Ungera, L.-S.; Niedrig, C.; Wagner, S.F.; Menesklou, W.; Baumann, S.; Meulenberg, W.A.; Ivers-Tiffée, E. Yttrium doping of $Ba_{0.5}Sr_{0.5}Co_{0.8}Fe_{0.2}O_{3-\delta}$ part I: Influence on oxygen permeation, electrical properties, reductive stability, and lattice parameters. *J. Eur. Ceram. Soc.* **2018**, *38*, 2378–2387. [CrossRef]
37. Wei, B.; Lü, Z.; Li, S.; Liu, Y.; Liu, K.; Su, W. Thermal and Electrical Properties of New Cathode Material $Ba_{0.5}Sr_{0.5}Co_{0.8}Fe_{0.2}O_{3-\delta}$ for Solid Oxide Fuel Cells. *Electrochem. Solid-State Lett.* **2005**, *8*, A428–A431. [CrossRef]
38. Naumkin, A.V.; Kraut-Vass, A.; Gaarenstroom, S.W.; Powell, C.J. *NIST X-ray Photoelectron Spectroscopy Database, NIST Standard Reference Database 20 (Version 4.1)*; US Department of Commerce: Washington, DC, USA, 2012. [CrossRef]

39. Kao, W.-X.; Lee, M.-C.; Lin, T.-N.; Wang, C.-H.; Chang, Y.-C. Fabrication and characterization of a $Ba_{0.5}Sr_{0.5}Co_{0.8}Fe_{0.2}O_{3-\delta}$-Gadolinia-doped ceria cathode for an anode-supported solid-oxide fuel cell. *J. Power Sources* **2010**, *195*, 2220–2223. [CrossRef]
40. Li, J.; Yang, C.; Liu, M. High performance intermediate temperature solid oxide fuel cells with $Ba_{0.5}Sr_{0.5}Co_{0.8}Fe_{0.1}Nb_{0.1}O_{3-\delta}$ as cathode. *Ceram. Int.* **2016**, *42*, 19397–19401. [CrossRef]
41. Duan, Z.; Yang, M.; Yan, A.; Hou, Z.; Dong, Y.; Chong, Y.; Cheng, M.; Yang, W. $Ba_{0.5}Sr_{0.5}Co_{0.8}Fe_{0.2}O_{3-\delta}$ as a cathode for IT-SOFCs with a GDC interlayer. *J. Power Sources* **2006**, *160*, 57–64. [CrossRef]
42. Yang, Z.; Yang, C.; Xiong, B.; Han, M.; Chen, F. $BaCo_{0.7}Fe_{0.2}Nb_{0.1}O_{3-\delta}$ as cathode material for intermediate temperature solid oxide fuel cells. *J. Power Sources* **2011**, *196*, 9164–9168. [CrossRef]

© 2020 by the authors. Licensee MDPI, Basel, Switzerland. This article is an open access article distributed under the terms and conditions of the Creative Commons Attribution (CC BY) license (http://creativecommons.org/licenses/by/4.0/).